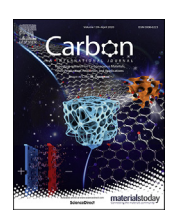
ELSEVIER

Contents lists available at ScienceDirect

Carbon

journal homepage: www.elsevier.com/locate/carbon



Maleic anhydride-functionalized graphene nanofillers render epoxy coatings highly resistant to corrosion and microbial attack



Govinda Chilkoor ^{a, b}, Roman Sarder ^c, Jamil Islam ^a, K.E. ArunKumar ^d, Ishara Ratnayake ^e, Shane Star ^a, Bharat K. Jasthi ^f, Grigoriy Sereda ^c, Nikhil Koratkar ^{g, h}, M. Meyyappan ⁱ, Venkataramana Gadhamshetty ^{a, b, *}

- ^a Department of Civil and Environmental Engineering, South Dakota School of Mines and Technology, 501 E Saint Joseph Blvd, Rapid City, SD, 57701, United States
- ^b 2-Dimensional Materials for Biofilm Engineering Science and Technology (2DBEST) Center, South Dakota School of Mines and Technology, 501 E. St. Joseph Street, Rapid City, SD, 57701, United States
- ^c Department of Chemistry, University of South Dakota, 414 E. Clark St, Vermillion, SD, United States
- d Department of Chemical and Biological Engineering, South Dakota School of Mines and Technology, 501 E Saint Joseph Blvd, Rapid City, SD, 57701, United States
- e Department of Nanoscience and Nanoengineering, South Dakota School of Mines and Technology, 501 E Saint Joseph Blvd, Rapid City, SD, 57701, United States
- f Department of Materials and Metallurgical Engineering, South Dakota School of Mines and Technology, 501 E Saint Joseph Blvd, Rapid City, SD, 57701, United States
- g Department of Mechanical, Aerospace and Nuclear Engineering, Rensselaer Polytechnic Institute, 110 Eighth Street, Troy, NY, 12180-3590, United States
- h Department of Chemical and Biological Engineering, Rensselaer Polytechnic Institute, 110 Eighth Street, Troy, NY, 12180-3590, United States
- ¹ Center for Nanotechnology, NASA Ames Research Center, Moffett Field, Mountain View, CA, 94035, United States

ARTICLE INFO

Article history:
Received 4 October 2019
Received in revised form
21 December 2019
Accepted 23 December 2019
Available online 29 December 2019

Keywords: Diels—Alder reaction Microbiologically induced corrosion Functionalized graphene Nanofillers

ABSTRACT

Iron-based alloys that are ubiquitously used in industrialized societies are prone to corrosion which results in large maintenance and repair costs. Here we design maleic-anhydride-functionalized graphene nanofillers to enhance corrosion resistance of epoxy coating (MAGE) on mild steel surfaces, with a corrosion protection efficiency of 99.9%. A mechanochemical approach based on Diels-Alder reaction was used to synthesize graphene nanofillers and functionalize them with difunctional bisphenol A/epichlorohydrin epoxy. The MAGE coating increased corrosion resistance of steel by 9–10 orders of magnitude compared to bare metal in both abiotic (3.5% NaCl) and aggressive microbial (sulfate-reducing bacteria, SRB) environments. Compared to unfunctionalized graphene nanoplatelets, the MAGE coating offered four orders of magnitude lower corrosion resistance against planktonic SRB cells, 80% lower against sessile SRB cells, and 19-fold lower against 3.5% NaCl. The unique functional groups in maleic-anhydride-graphene adducts enabled their dispersion in epoxy coating and enhanced its mechanical properties. The high corrosion resistance of MAGE in diverse environments is attributed its outstanding ability to block the intercalation of corrosive species.

© 2019 Elsevier Ltd. All rights reserved.

1. Introduction

Iron alloys that are widely used in marine sector, oil and gas industry, utilities, transportation [1,2] are susceptible to both corrosion and microbiologically influenced corrosion (MIC) [3]. For

E-mail address: Venkata.Gadhamshetty@sdsmt.edu (V. Gadhamshetty).

example, sulfate reducing bacteria (SRB) attack steel pipelines that represent a transmission network that carries crude oil, natural gas as well as saline forms of oil and gas wastewater. Pitting corrosion and MIC could cause pinhole leaks in these oil and gas pipelines induce spills to cause negative environmental impacts [4]. While MIC accounts for 20% of the total direct corrosion costs in the U.S (\$1 trillion), SRB alone contributes to \$5 billion of these costs [5–7]. Although polymers coatings work effectively under abiotic conditions, they tend to fail under aqueous and microbial conditions. SRB biofilms degrade polymers. They cause wear, surface abrasion and

^{*} Corresponding author. Department of Civil and Environmental engineering, South Dakota School of Mines and Technology, 501 E Saint Joseph Blvd, Rapid City, SD, 57701, United States.

volume shrinkage, induce defects and cracks [1,6] and facilitate seepage of corrosive ions [1,6]. It remains a long term challenge to design a coating that works effectively in both abiotic and biotic environments.

This study discusses an approach to introduce a network of interconnecting filler molecules to seal inherent defects in polymer coatings, for example those induced during the cure shrinkage step of the fabrication process [8,9]. Commercial fillers that are typically required at higher levels (60% v/v) could reduce tensile strength and flexural properties of the polymers [9,10]. Here we establish that nanofillers based on maleic-anhydride-functionalized graphene (MAG) adducts (<1% v/v) (referred to as nanofillers) greatly improve both the corrosion resistance and MIC resistance of epoxy coatings without compromising their functional strength. Such functionalization strategies decrease the surface energy of graphene and improve their dispersion in base polymers [10,11]. They can also tune surface roughness, wettability and antibacterial properties of metal surfaces and control the biofilm growth [12,13].

The edges of graphene could be anchored with functional groups via non-covalent or covalent methods to enable dispersion of graphene in base polymers [14,15]. The non-covalent methods involve π – π interactions or ionic interactions while covalent methods involve chemical functionalization. Non-covalent methods retain the structural quality of pristine graphene, but they are not necessarily suitable for biological applications [10]. Chemical functionalization strategies entail use of toxic chemicals (e.g., ammonia) [16,17].

Earlier studies have used Zn [18], Ag—TiO₂ [19] and graphene oxide [20] as the nanofillers to enhance biocidal activity [21] and antibacterial properties [22] of polymers. Such polymer composites could resist the adhesion of bacterial cells [[20,23,24]]. To the best of the authors' knowledge, none of these nanofillers were explored for use in MIC applications. Furthermore, the use of mechanochemically exfoliated graphene proposed in this study were never considered for tuning MIC resistance of polymers. Here we establish that epoxy coatings modified with 0.25% w/w of MAG nanofillers (herein referred as MAGE coating) protect mild steel exposed to SRB which are widely implicated in MIC.

We present a facile ball milling process for mechanochemically exfoliating graphene particles and simultaneously functionalizing them with maleic anhydride. This process operates under ambient conditions and it obviates the use of harsh chemicals such as hydrazine hydrate typically used for exfoliating graphene. The MAGE coatings could prevent abiotic corrosion as well as MIC, without the need for biocides used to control growth of SRB cells . Such coatings can be expected to offer life cycle analysis (LCA) sustainability benefits [25]. Our earlier study demonstrated that graphene-polymer coatings that obviate the use of biocides could reduce the negative impacts (e.g., global warming, carcinogenicity and eutrophication potential) [26].

We used maleic anhydride as a dienophile to mechanochemically cleave inexpensive graphite substrate (diene) into MAG adducts which were dispersed in a cycloaliphatic amine curing agent, and finally mixed with bisphenol A/epichlorohydrin derived liquid epoxy resin to obtain MAGE coatings [27]. The carbonyl and hydroxyl in the MAG adducts enabled their dispersion in the epoxy matrix. The modulus and hardness values of MAGE were 6.3% higher compared to bare epoxy. We used electrochemical tests to demonstrate that the MAGE coating on mild steel enhances corrosion resistance by nine to ten orders of magnitude compared to uncoated steel and by five-fold compared to epoxy-coated steel, under both abiotic and biotic conditions. The MAGE coating offered high corrosion protection efficiency (99.9%) when compared to epoxy coating (91%), even after 40 days of continuous exposure to SRB biofilms. The resulting imide functional groups in MAGE

enhanced its moisture barrier properties and overall hydrophobicity [2]. Microscopy tests, MD simulations and electrochemical impedance spectroscopy analysis confirm that MAGE forms an impermeable barrier on mild steel to protect it against aggressive metabolites.

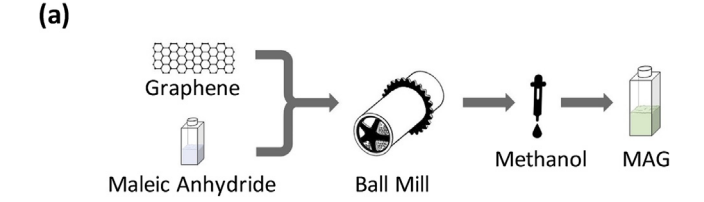
2. Experimental section

2.1. Materials

Maleic anhydride, graphite and methanol used to synthesis MAG were purchased from Sigma Aldrich and they were used without further treatment. The cycloaliphatic amine (EPIKURE™ Curing Agent 3387) and difunctional bisphenol A/epichlorohydrin epoxy resin (EPON™ Resin 828) were obtained from Hexion (Houston, Texas). AISI 1018 mild steel (Fe: 99.72%; C: 0.21%; Mn: 1.03%; Si: 0.2%; Ni: 0.06%; Cu: 0.17%; and Al: 0.03%) were purchased from McMaster-Carr was used as the working electrode in all of the corrosion tests. The electroplating mask used to limit the working electrode exposure area to 1 cm² was obtained from Gamry Instruments (990−00254). The silicon carbide papers used for polishing mild steel from 240 up to 1200 grit was obtained from Page technologies (SIP−P08C).

2.2. Synthesis of MAG adducts and MAGE mixture

The MAGE was synthesized using a two-step process (Fig. 1a and b). MAG adducts were prepared by ball milling the maleic anhydride and graphite particles (1:2 w/w) at 500 rpm for 48 h in a vacuumed ball mill (Fig. 1a). The resulting MAG adducts were



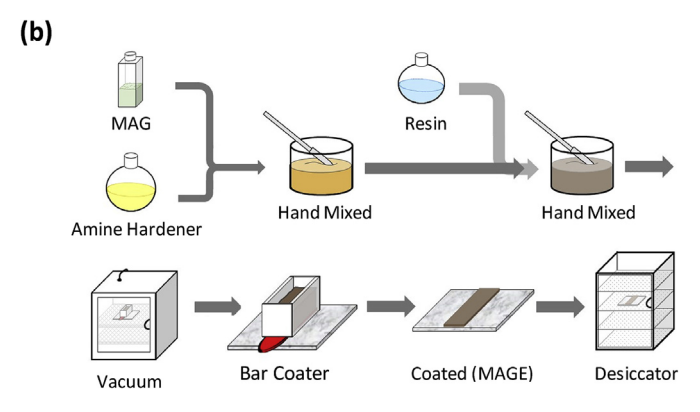


Fig. 1. (a) Synthesis of maleic-anhydride-functionalized graphene (MAG) nanofillers via ball milling of graphite in presence of maleic anhydride. An insitu Diels—Alder reaction between graphene edges (diene) and maleic anhydride (dienophile) yielded MAG nanoplatelets. (b) Preparation of MAGE coating and its application on mild steel. MAG nanoplatelets (0.25 wt %) dispersed in cycloaliphatic amine was mixed with difunctional bisphenol A/epichlorohydrin derived liquid epoxy resin to form MAGE mixture. The MAGE mixture was left in vacuum drier to remove air bubbles before it was coated on the mild steel coupon. The MAGE coated mild steel was left in a desiccator for 7 days before carrying out microbial corrosion test mechanochemically driven solid-state Diels—Alder reaction between in situ generated active carbon species by ballmilling in the presence of a specific dienophile, maleic anhydride (MA) or maleimide.

washed with methanol to separate the unreacted graphene from the functionalized graphene. The MAG powder (0.25 wt %) was then mechanically mixed with 5 g of cycloaliphatic amine curing agent for 5 min. The resulting mixture was dispersed in 5 g of difunctional bisphenol A/epichlorohydrin derived liquid epoxy resin by mechanically stirring the two components for 5 min to obtain MAGE. The epoxy mixture (a control for MAGE) was obtained by mechanically mixing difunctional bisphenol A/epichlorohydrin derived liquid epoxy resin with cycloaliphatic amine hardener (1:1) for 5 min. The MAGE and epoxy mixtures were treated individually in a vacuum oven at room temperature for 2 min to remove any air bubbles.

2.3. Application of MAGE and epoxy coatings on mild steel

MAGE or epoxy coatings were applied on the surface of 1018 mild steel (MS) using a high precision baker film applicator (Elcometer Model 3525) set to a thickness gap of 30 μ m (Fig. 1b). The coated samples were dried at 25 °C for 7 days in a desiccator prior to their use in corrosion tests. The MAGE and epoxy coated mild steel surfaces are herein referred as MAGE-MS and epoxy-MS, respectively.

2.4. Characterization

The graphite and as-synthesized MAG were characterized using Powder X-ray diffraction (PXRD) (Rigaku Ultima IV) and the XRD data was processed using the PDXL2 software. The samples were further characterized using Fourier transform infrared spectroscopy (FTIR) (PerkinElmer) in the spectrum range of $400-4000~\rm cm^{-1}$ using the KBr pellet method discussed elsewhere [27]. The FTIR spectrum data was processed using the Spectrum 2 software.

The morphology of MAG fillers was evaluated using a Zeiss Sigma scanning electron microscope (SEM). Prior to the observation, 5 mg of the MAG samples were dissolved in 10 mL of hexane, drop casted on a clean silicon wafer and finally dried at room temperature. The dried samples were rinsed in hexane and airdried before placing it in Zeiss Supra 40 SEM. Transmission electron microscope (TEM) was used to further assess the topography, lateral size and the number of layers of the MAG sheets. TEM analysis was carried out by placing a drop of MAG/methanol dispersion on to a carbon-coated 200 mesh copper grid.

The dispersion of the MAG fillers in epoxy was qualitatively assessed using TEM analysis. The MAGE and epoxy samples were first cut into sections (70 nm thick) with an ultramicrotome (RMC Powertome XL). The TEM images of the cross-section were acquired using a JEOL JEM-2100 LaB6. Thermogravimetric analysis (TGA, Q 400; T.A instruments, New castle, DE) was used to study thermal stability of the epoxy and MAGE coatings in a nitrogen atmosphere. TGA analysis was carried out in the temperature range of 29 °C-720 °C and with a ramp rate of 10 °C/min. Raman spectra was used to analyze graphite and MAG samples using ffTA Foram ×3 module (Foster + Freeman Ltd, Evesham, UK) with a lens magnification of 5x, a laser excitation wavelength of 638 nm, incident power of 10 mW and in the spectral range of 400–3700 cm⁻¹. The wettability of the MAGE and epoxy coatings was evaluated by a contact angle goniometer (Model 500, raméhart Instrument Co.). The water droplets were analyzed by DROPimage Advanced v 2.4 software to estimate the water contact angle. The nanoindentation experiments were carried out using an MTS Nanoindenter® XP with a load and displacement resolution of 0.05 µN and 0.01 nm, respectively. A standard diamond Berkovich indenter with a half angle of 65.35° and tip radius of 150 nm was used. Multiple indentations were performed at the rate of 5 mN/s up to a maximum load of 75 mN, held for 15 s and then decreased to zero at the same rate.

To observe the biofilm on the surface of coated samples, a fixation protocol described in our earlier study was used prior to the SEM examination [5]. Energy dispersive spectroscopy (EDS) (Oxford Aztec Energy advanced system) analysis was used to obtain chemical composition of the biofilm and associated corrosion products. The corrosion products were characterized using an Ultima-Plus X-ray diffractometer (XRD, Rigaku, Japan) and the data were analyzed using the Jade 7.5 software.

2.5. Incubation of sulfate reducing bacteria

The growth procedures described in our earlier studies [6] were used to preculture *Desulfovibrio alaskensis* G20 in sterilized Lactate C medium consisting of the following constituents (g/L): sodium lactate, 6.8; sodium sulfate, 4.5; sodium citrate, 0.3; dehydrated calcium chloride, 0.06; ammonium chloride, 1.0; magnesium sulfate, 2.0; potassium phosphate monobasic, 0.5 and yeast extract). The media was sterilized in an autoclave at 121 °C for 30 min. Cultures were grown in 150 mL sealed serum bottles containing 100 mL of the sterilized L-C media and N_2 – O_2 headspace (9:1 v/v). *D. alaskensis* cultures were incubated at 30 °C and with an agitation speed of 125 rpm for 48 h using an orbital platform shaker.

2.6. Corrosion tests and microbiologically influenced corrosion experiments

All corrosion experiments were carried out in a three-electrode corrosion cells using the Lactate C medium containing *Desulfovibrio alaskensis* G20 as the electrolyte (biotic) and 3.5% NaCl as the electrolyte (abiotic). Silver/silver chloride/saturated KCl (Ag/AgCl) was used as the reference electrode, and graphite plate as counter electrode. Standard microbiology practices and sterile techniques discussed in our earlier study [6] were used to carry out the MIC experiments for 40 days.

2.7. The electrochemical measurements and calculations

A Gamry Reference 600 potentiostat was used to carry out the linear polarization resistance (LPR) tests and EIS experiments after achieving a stable open circuit potential (OCP). LPR tests were run in triplicates with an applied voltage of ± 10 mV (vs. OCP) and at a scan rate of 0.125 mV/s. The slope of the current-versus-voltage curve was used to calculate the polarization resistance ($R_{\rm p}$). The $R_{\rm p}$ was then used in the Stern-Geary equation to determine the corrosion current ($i_{\rm corr}$) using equation (1), and corrosion rate using equation (2).

$$i_{corr} = \frac{\beta_a \beta_c}{(\beta_a + \beta_c)} \times \frac{1}{2.3R_p} = \frac{B}{R_p}$$
 (1)

where βa and βc are the anodic and cathodic Tafel constants, respectively and were obtained from Tafel analysis; and B is the Stern-Geary coefficient.

Corrosion rate
$$(mpy) = \frac{K.EW.i_{corr}}{d.A}$$
 (2)

where EW and d are the equivalent weight (25.12 g/equivalent) and density (7.9 g/cm³) of mild steel respectively, A is the exposed sample area in cm² and K is the conversion factor (1.288 \times 10⁵ milliinches (A-cm-year)) to obtain the corrosion rate in mpy. The EIS tests were carried out in the frequency range of 100 kHz to 10 mHz with signal amplitude perturbation of 10 mV. The impedance data

were analyzed using Gamry Echem analyst software.

2.8. Molecular dynamic (MD) simulations

We used a Forcite module in the Materials Studio 2018 program to carry out MD simulations and probe the structural basis for the stability of MAG. The Condensed phase Optimized Molecular Potentials for Atomistic Simulation Studies (COMPASS) forcefield technology was used to conduct geometric optimization of MAG obtained via Diels-Alder reaction.

3. Results and discussion

3.1. Synthesis and characterization of MAG

Fig. 1a and b depicts the facile route used to synthesize MAGE coating. The graphite along with maleic anhydride was ball milled to promote the Diels-Alder [4+2] cycloaddition reaction. The ball milling enabled an in-situ exfoliation of graphene nanoplatelets (conjugated diene) from the graphite, broke the edges of the carbon rings to yield active sites for anchoring maleic acid functional groups (dienophile), and ultimately bonded the 4π -electrons of the conjugated diene with 2π -electrons of the dienophile.

The MAG samples were characterized using SEM, TEM, PXRD, FT-IR and Raman. The SEM tests were used to compare the surface topography of pristine graphite with MAG. The graphite sheet shows a smooth surface without any corrugation (Fig. 2a). In

contrast, the MAG exhibit a rough texture (Fig. 2b) in the form of wrinkles and corrugations, primarily due to stacking of exfoliated graphene sheets (Fig. 2b inset). The higher resolution TEM tests were used to assess the lateral size (Fig. 2c) and thickness of MAG nanofillers (Fig. 2d). The lateral size of MAG sheets ranged from 0.6 μ m to 1.5 μ m (Fig. 2c) and the average thickness was 3.95 nm (Fig. 2d). These dimensions are smaller compared to the lateral size of graphite flakes (500 μ m). The visible and clear rings in selected area electron diffraction pattern (inset of Fig. 2c) confirm the presence of crystalline multilayered graphene. These results imply that the graphitic planes were reduced to multilayered graphene sheets during the ball milling process.

Fig. 2e reveal the powder X-ray diffraction pattern of the MAG particles. The spacing between graphene layers (\sim 1.72 Å, $2\theta=26.7^{\circ}$) in MAG matches with the parent graphite, which corroborates the multilayered morphology of exfoliated graphene. The intensity of these reflections is lower than that of pristine graphene, reflecting the smaller dimensions of the ball-milled MAG particles. A phase with a smaller distance between the graphene planes (1.62 Å, $2\theta=28.4^{\circ}$) in MAG confirms the hydrogen bonding between the carboxy-groups formed during hydrolysis [28].

The functional groups in MAG were identified using FT-IR spectroscopy (Fig. 2f). The strong absorption at ~1700 cm⁻¹ is a characteristic of the stretching C=O vibration which occurs below the characteristic value of the anhydride (1758 cm⁻¹). This result points to the hydrolysis of the anhydride ring. The moderate band at 1758 cm⁻¹ refers to the remaining anhydride moieties. The

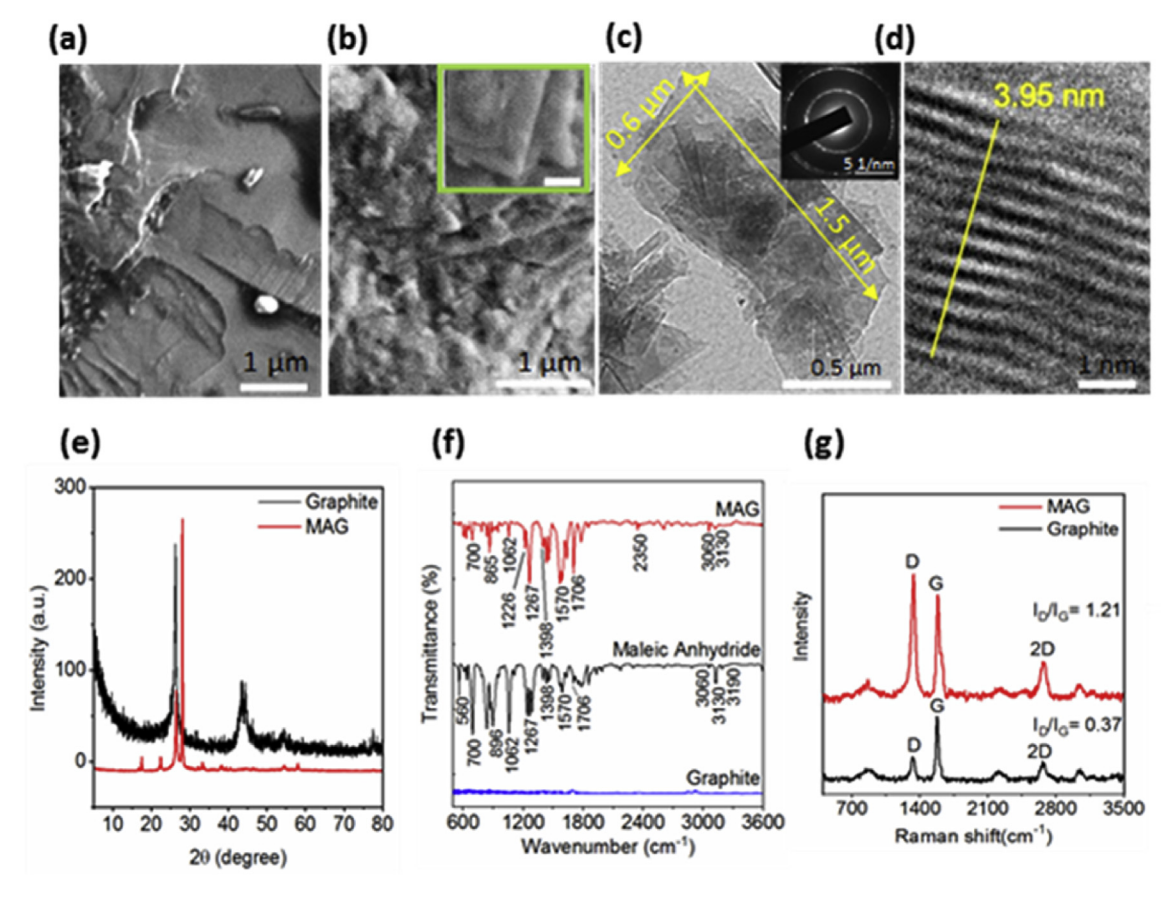


Fig. 2. Characterization of Maleic anhydride functionalized graphene (MAG). SEM micrographs for (a) pristine graphite and (b) MAG. The inset SEM image shows stacked sheets of graphene in MAG. Scale bar: 500 nm. TEM micrographs of (c) MAG and its corresponding electron diffraction pattern (inset) (d) the cross-section of MAG. (e) Powdered X-ray diffraction pattern shows a characteristic peak of graphite at $2\theta = 26.50$ for (002) plane having a d-spacing of 3.37 Å and another characteristic peak at $2\theta = 540$ for (004) plane having d-spacing of 1.69 Å. (f) The full FTIR spectra of MAG shows a strong band at 1570 cm-1 which is characteristic for C=C bond stretching at the edge of graphene.(g) Raman spectra for MAG showing higher D band intensity compared graphite confirming the higher degree of functionalization. (A colour version of this figure can be viewed online.)

absorption band at ~3098 cm $^{-1}$ characterizes C (sp 2)-H stretching vibrations and points out that certain maleic-anhydride-acylated OH groups are available at the oxidized edges of MAG. We did not observe any signs of multiple reflection characteristics that are typical to maleic anhydride [29]. The C (sp 2)-H stretching bands pattern for maleic anhydride is significantly different compared to MAG. A series of bands observed at 1200-1285 cm $^{-1}$ (different compared to maleic anhydride) signifies the presence of C–O bonds.

Raman spectra in Fig. 2g confirms the presence of graphene in MAG. As expected, the graphite samples display the typical lower intensity D band (1326 cm $^{-1}$) along with a G band (1570 cm $^{-1}$) and 2D band (2680 cm $^{-1}$). A strong D band intensity at 2670 cm $^{-1}$ for MAG suggests it is characterized by enhanced edge defects. The I_D/I_G ratio [14] for MAG (1.21) is 3.2-fold higher than pristine graphite ($I_D/I_G = 0.37$), suggesting the formation of covalent bond and noncovalent complexation [16]. The functionalization of graphene edges occurs via covalent functionalization (cycloaddition) while that of the basal plane favors noncovalent complexation [16]. The MD simulation tests presented in the supporting information confirm that the cycloaddition reaction occurs at the armchair edges versus the basal graphitic plane (Figs. S1-3) [27].

3.2. Characterization of MAGE coating

As shown in Fig. 1b, the MAG adducts were mixed with the amine hardener prior to its incorporation in the epoxy resin. An interfacial reaction between the nitrogen atom in the amine group (of the amine hardener) and carbonyl group (of the MAG) promoted the formation of the imides (N-C=O and C-N groups) [30]. The curing process enabled a cross linking reaction between the imidefunctionalized MAG containing amine groups and epoxide groups of epoxy resin. As reported in ref [31], the IR analysis does not necessarily capture the undetectable levels of the imide grafts, especially due to the low levels of MAG (0.25 wt %) used to modify the epoxy. However, a study by Zabihi Omid et al. confirmed that MAG reacts with amine groups to form the imides group [31]. Such imide groups increase the hydrophobicity of polymers coating [32]. We have observed that MAG nanofillers enhanced hydrophobicity of epoxy coating, inferring the formation of the imide groups [32,33]. As discussed in the latter sections, the hydrophobic MAGE coating was characterized by enhanced MIC resistance.

TEM images shows homogenously distributed aggregates of MAG in the epoxy matrix with a lateral size of 0.5 μ m-3 μ m (Fig. 3a). The absence of voids indicates its favorable interaction with epoxy. The SAED in the inset of Fig. 3a confirms the presence of multilayered graphene in the MAG aggregates. The SEM images in Fig. 3b and c shows the surface and morphological characteristics of the epoxy-MS and MAGE-MS substrate respectively. The inset images in Fig. 3b and c shows the optical images of the cross section of epoxy-MS and MAGE-MS. It is evident from the cross-sectional images that the MAG is well-layered in MAGE-MS. These results confirm that the ball milling process yielded functionalized graphene edges and forms MAG adducts that disperse in the epoxy matrix without forming agglomerates [27]. This finding is noteworthy considering the previously reported agglomeration issues when graphene fillers were dispersed in base polymer matrix [34].

To assess if the MAG nanofillers enhance the thermal stability of epoxy coatings, we compared the results of the TGA analysis for the MAGE and epoxy at 120 °C to 700 °C (Fig. 3d). The upper ceiling for this temperature range is three-fold higher than the boiling point of epoxy coatings (177 °C). As such this TGA analysis reveals the true contributions of the MAG nanofillers to exceptional performance of MAGE coatings. As shown in Fig. 3d, the MAGE is thermally stable compared to neat epoxy, evident from the lower weight loss at

400–550 °C and higher char yield (15%) at 700 °C. Both MAGE and epoxy remained stable below 120 °C. However, unlike epoxy coatings, the MAGE exhibited an initial weight loss at 100 °C and 400 °C due to the thermal decomposition of the functional groups, corroborating the presence of the edge functional groups in MAGE [27].

Nanoindentation testing confirmed that the MAG nanofillers increased the mechanical properties (hardness and modulus) of the epoxy coatings (Fig. 3e). The analysis using the Oliver and Pharr method revealed that at maximum load the average values of modulus and hardness of the MAGE coating were 3.93 GPa and 148 GPa, and that of epoxy were 3.83 GPa and 138 GPa. These results show that MAGE registered an increase of at least 6.3% in both the modulus and hardness values.

Contact angle measurements for epoxy-MS and MAGE-MS confirm that MAG fillers enhanced the hydrophobicity of epoxy coatings (Fig. 3f). Hydrophobic surfaces are typically characterized by water contact angle values greater than 90° [4]. The water contact angle for MAGE-MS ($90^\circ \pm 2$) was 10° and 19° higher compared to epoxy-MS ($80 \pm 2^\circ$) and bare MS ($71 \pm 2^\circ$), respectively. The enhanced hydrophobicity is due to the formation of imide group during the reaction between MAG and epoxy [9].

3.3. High performance MAGE coatings for protecting mild steel exposed to SRB biofilms

We assess the MIC resistance of MAGE coatings on mild steel exposed to biogenic sulfide corrosion effects of Desulfovibrio alaskensis G20. The performance of MAGE-MS was first compared with bare mild steel. As shown in Fig. 4a, the MAGE-MS stayed intact even after 40 days of continuous exposure to SRB-G20 while the bare mild steel exhibited distinct signs of corrosion. The SEM images of the exposed bare mild steel (Fig. 4b) showed clusters of rodshaped SRB-G20 cells and their biofilm, while MAGE-MS did not show any signs of biofilm attachment. The MIC resistance of MAGE coatings was quantitatively established using both the potentiodynamic polarization tests and EIS analysis. Fig. 4c show the potentiodynamic polarization curves of the bare mild steel and MAGE-MS after 40 days of exposure to SRB-G20. Based on the Tafel fit, the corrosion current densities (icorr) and corrosion rates (mpy) for MAGE-MS (135 \times 10- μA cm⁻²; 55 \times 10⁻⁶ mpy) were three orders of magnitude lower compared to uncoated MS (302 \times $10^{-3} \,\mu\text{A cm}^{-2}$; $123 \times 10^{-3} \,\text{mpy}$) (Fig. 4c; Table S1). The corrosion potential ($E_{corr} = 400 \text{ mV}$), the intercept of the anodic and cathodic regions of the plot (Fig. 4c) was also more positive for MAGE-MS compared to bare mild steel. The higher the positive value of E_{corr} the lower is the corrosion susceptibility. These series of results confirm that MAGE coatings inhibit iron dissolution from the mild steel surfaces exposed to SRB-G20.

After quantitatively elucidating corrosion rates, the EIS techniques were used to investigate the microbial corrosion protection mechanisms of MAGE coating (Fig. 4d). As shown in the Bode impedance plots and phase angle plots, MAGE-MS exhibits higher charge transfer resistance and phase angle compared to uncoated MS. This finding provides a first line of evidence to establish barrier properties of MAGE coatings. The absolute impedance modulus at low frequency of 0.01 Hz ($|Z|_{0.01\text{Hz}}$) was five orders of magnitude higher for MAGE coatings compared to the uncoated MS. The absolute impedance is the square root of the sum of squares of real impedance (Z_r) and imaginary impedance (Z_i) (Equation (3)) [35,36]. The phase angle at the higher frequency for MAGE-MS was -60° while the uncoated MS exhibited a phase angle of 0° after exposure for 40 days (Fig. 4d).

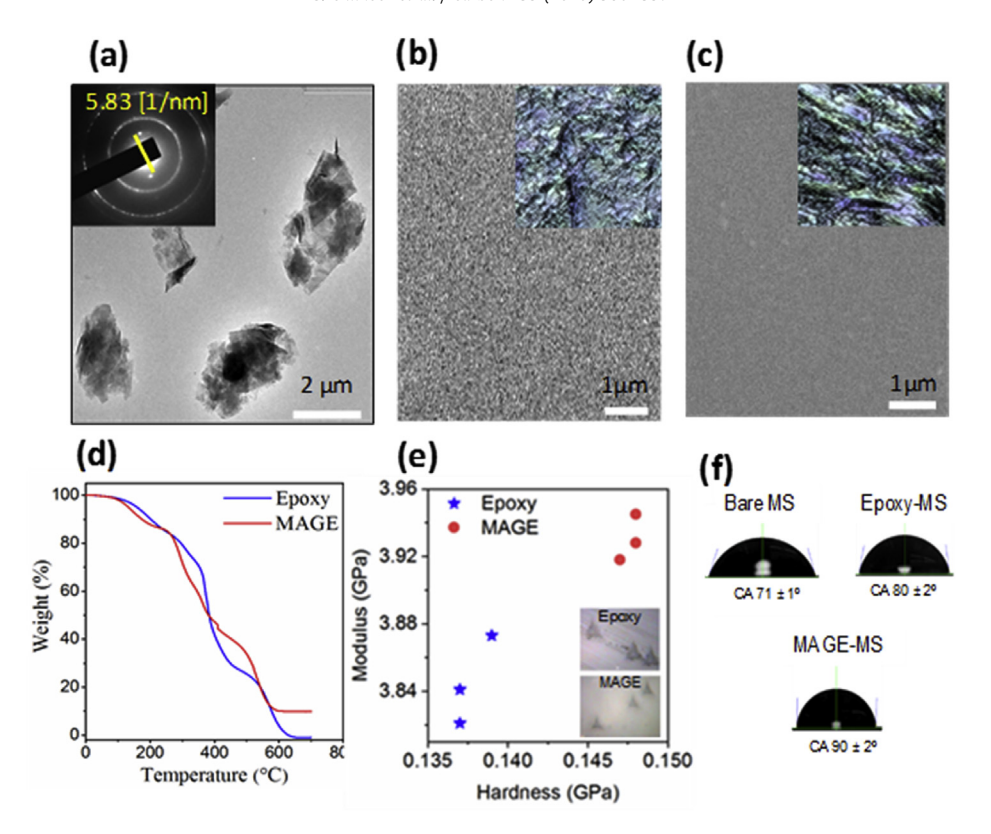


Fig. 3. Characterization of maleic anhydride functionalized graphene -epoxy composite (MAGE). (a) TEM image show dispersion of MAG in epoxy matrix. Inset confirms graphene layers in MAGE as represented by the electron diffraction pattern with a 2 d value of 5.83 [1/nm] which corresponds to a d-spacing of 0.34 nm. SEM images of coated samples for (b) epoxy-MS and (c) MAGE-MS. (d) TGA thermograms obtained at heating rate of 10 °C/min in nitrogen atmosphere. MAGE show higher thermal stability compared to epoxy. This is evident from its lower weight loss at 400–550 °C and higher char yield (15%) at 700 °C. (e) Nanoindentation tests show a 6% increase in hardness and modulus for MAGE compared to epoxy (at maximum load). The inset shows the three nanoindentation marks on the epoxy and MAGE samples (f) Contact angle measurements shows that MAG nanofillers yield hydrophobic MAGE coatings. (A colour version of this figure can be viewed online.)

$$Z_{mod} = \sqrt{Z_r^2 + Z_i^2} \tag{3}$$

The EIS results suggest that the protective mechanism of MAGE coating is due to its resistive and capacitive behavior.

3.4. MAG nanofillers enhance barrier properties of epoxy coating exposed to SRB

To assess the contribution of MAG nanofillers to the exceptional barrier property of MAGE coating, we compared the MIC resistance of MAGE coating with its commercial counterpart namely epoxy coatings. We evaluate the temporal performance of the two coatings for nearly 40 days of continuous exposure to the biogenic sulfate reducing conditions. To enable a fair comparison, both the coatings were obtained at an identical thickness of 30 μm . The following results generated from the two different techniques establish the superior MIC resistance of MAGE coating compared to commercial epoxy coatings.

The nobler open circuit potential values of MAGE-MS (Fig. 5a) compared to epoxy-MS indicate that the MAG nanofillers at a low loading rate (0.25 wt%) have effectively improved the MIC resistance of epoxy coatings. As shown in Fig. 5a, the MAGE-MS display a nobler potential compared to epoxy-MS throughout the 40 days of SRB biofilm experiments. The peak value of the OCP for MAGE-MS (-200 mV vs. Ag/AgCl; obtained on day 40) was more positive compared to the least value of the OCP for epoxy MS (-655 mV vs. Ag/AgCl; observed on Day 1).

We used the non-destructive LPR technique for discerning the

instantaneous corrosion kinetics at the MS/coating/biofilm/electrolyte interface. The MAGE-MS displays (Fig. 5b) lower corrosion rate compared to epoxy-MS throughout the temporal scale. For example, the corrosion rates of MAGE-MS on day 40 (2.62 \times 10 $^{-4}$ mpy) was 22 times lower compared to epoxy-MS (5.76 \times 10 $^{-3}$ mpy). These findings imply that the uniformly dispersed MAG fillers with high surface area-per-unit-volume eliminating potential voids in epoxy coating and enhanced its barrier properties.

3.5. Microbial corrosion product analysis

To characterize the SRB-G20 biofilm and corrosion products on the epoxy-MS and MAGE-MS, we used SEM, EDS and XRD to carry out their postmortem analysis after 40 days of the exposure. The lower and higher magnification SEM images (Fig. 6a, c) for epoxy-MS show existence of dense rod-shaped SRB-G20 cells along with the corrosion products (FeS) which appear as the white deposits (Fig. 6a). In contrast, the MAGE-MS surfaces (Fig. 6b, d) did not develop any detectable levels of SRB-G20 biofilm and corrosion products. We highlight that the hydrophobic MAGE coatings discouraged attachment of SRB-G20 with a hydrophilic cell membrane [37–40]. Hydrophobic coatings reduce the contact area between the biological electrolyte and the coated surface.

To assess the nature of the biofilm-corrosion matrix, we obtained an EDS map for the region identified in the SEM images (Fig. 6e and f). The epoxy-MS surface (Fig. 6e) was characterized by higher levels of Fe (42.4%) compared to MAGE-MS (0.9%) (Fig. 6f). This result suggest that the MAG fillers minimize the diffusion of Fe²⁺ ions on to the metal surface. This result also matches with the

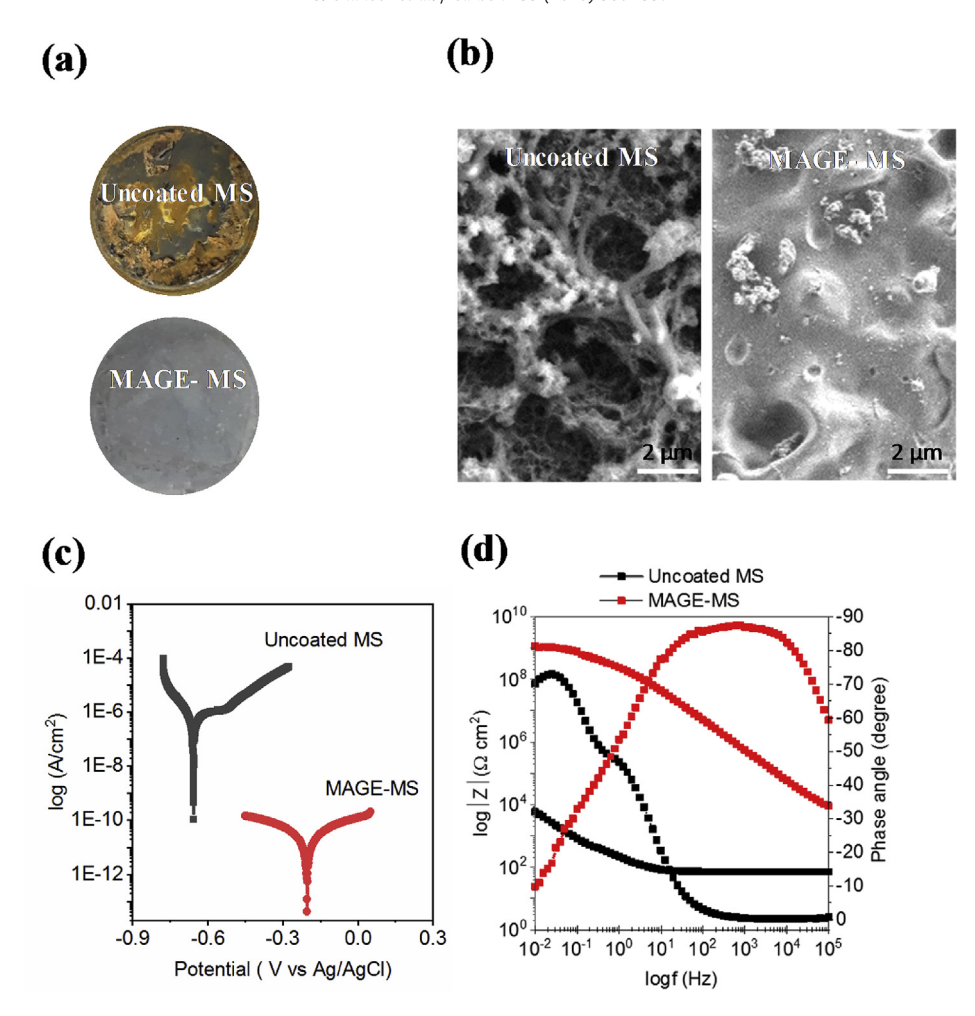


Fig. 4. Optical images and electrochemical analysis of Bare MS and MAGE-MS after 40 days of exposure to SRB-G20- (a) Optical and (b) SEM images for uncoated MS and MAGE-MS. Electrochemical test results showing (c) potentiodynamic polarization curves for uncoated MS and MAGE-MS. MAGE-MS shows suppressed anodic and cathodic current densities compared to uncoated MS. (d) ElS spectra represented in Bode impedance spectra for uncoated MS and MAGE-MS. The impedance (Log |Z|) at lower frequency (log f = 0.01 Hz) which is the total corrosion resistance (R_{corr}) for coatings, shows five order of magnitude higher for MAGE-MS compared to uncoated MS.

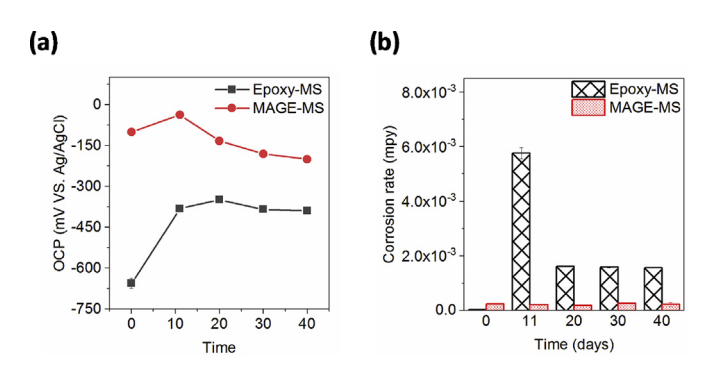


Fig. 5. DC corrosion test establish superior performance of MAGE compared to epoxy coatings. Temporal variation of (a) open circuit voltage and (b) corrosion rates derived from LPR measurements for epoxy-MS and MAGE-MS exposed to SRB-G20. (A colour version of this figure can be viewed online.)

lower R_c and higher capacitance values for the epoxy-MS from the EIS analysis, which is attributed to lower resistance to diffusion of corrosive ions. The sulfur peaks in EDS analysis indicates presence of biogenic hydrogen sulfide which dissociate to release protons (reaction 1) and increase the cathodic reduction kinetics or diffuse through the coating and react with Fe^o to form iron sulfide

(Equation (2)) [41].

$$H_2S^+ + 2e^- \rightarrow H_2 + 2HS^-(1)$$

$$Fe^{2+} + H_2S \rightarrow FeS + 2H^+(2)$$

3.6. Protective mechanisms of MAGE coatings

The MIC protection mechanisms of MAGE coatings in microbial environments were investigated using electrochemical impedance spectroscopy. Fig. 7a–c and Figs. S4a and b shows the Bode impedance and phase angle plots during the immersion period of 40 days. A time dependent variation of Bode plot captures the effect of SRB-G20 biofilm formation on the MIC resistance of the MAGE coating. In a Bode plot, the impedance value at the low frequency (| $Z|_{0.01~Hz}$) region gives a semi quantitative estimation of coating's barrier performance. MAGE-MS exhibited higher $|Z|_{0.01~Hz}$ values compared to epoxy-MS throughout the exposure times. The | $Z|_{0.01~Hz}$ on day 1 for MAGE-MS (1.725 \times 10¹⁰) was 10-fold higher compared to epoxy-MS (4.118 \times 10⁹) (Fig. 7a). On day 20 (Fig. 7b) and day 40 (Fig. 7c), the $|Z|_{0.01~Hz}$ values for MAGE-MS was at least two-orders of magnitude lower compared to compared to epoxy-

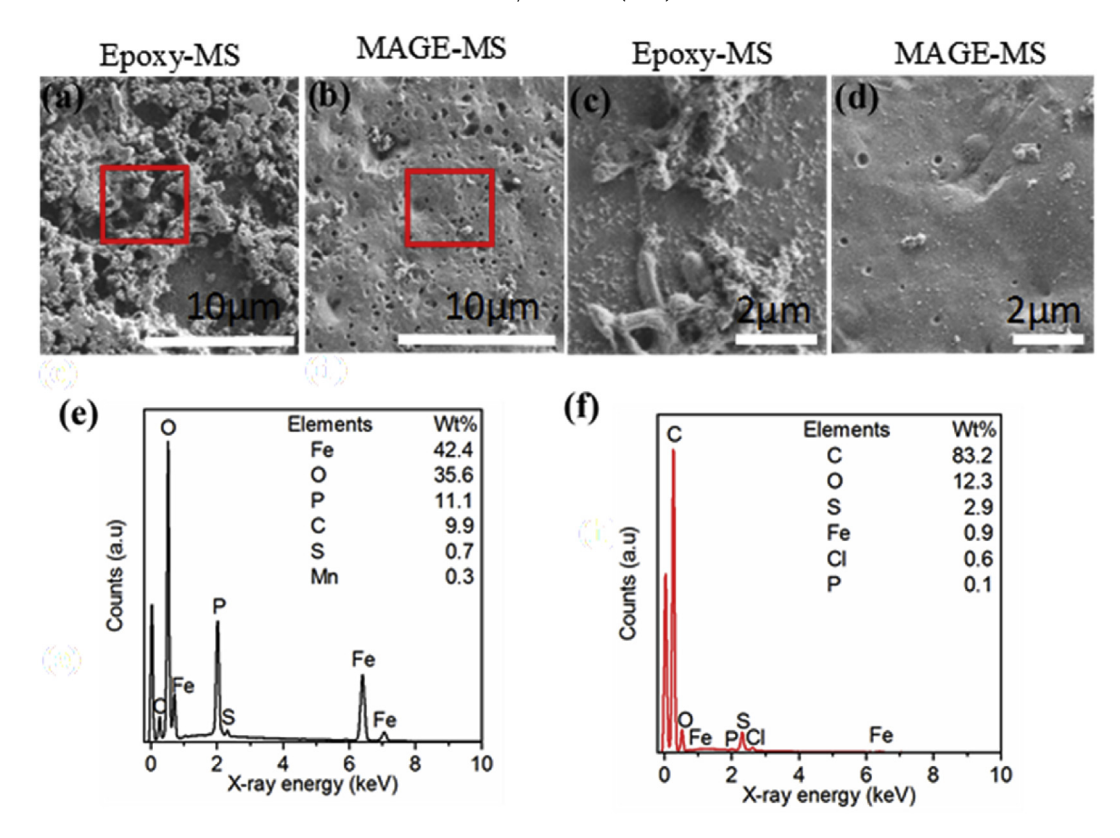


Fig. 6. SEM images of coated samples after 40 days of exposure to SRB G20. Lower magnification images for (a) epoxy-MS and (b) MAGE-MS; Higher magnification images of the area indicated in red (in Figure a and b) for (c) epoxy-MS and (d) MAGE-MS. SEM images shows lower adhesion of SRB-G20 cell and corrosion products for MAGE-MS compared to epoxy-MS; EDS map shows higher intensity Fe peaks for (e) epoxy-MS compared (f) MAGE-MS. The carbon peaks observed in EDS elemental analysis also includes the carbon used as conductive coating. (A colour version of this figure can be viewed online.)

MS.

Bode phase angle plots was further analyzed to understand the barrier coating performance of MAGE-MS. Bode phase angle plots reveal that MAGE-MS maintained a single broad phase angle curve extending from medium frequency range (10^0-10^2 Hz) to high frequency range (10^2-10^5 Hz) throughout the exposure time suggesting a robust coating (Fig. 7a,b,c). Generally, the onset of coatings failure would show distinct phase angle maxima evolving additional peaks with exposure time. The epoxy-MS showed a single broader phase angle plot on day 1 which later evolved into three narrowed phase angle maxima starting from day 10 revealing the onset of coating degradation. Starting day 30, the phase angle for epoxy-MS showed a an additional phase angle maxima peak in the high frequency range suggesting diffusion of ion transport (HS⁻) through the epoxy coating. The phase angle plots revealed that MAGE nanofiller strengthened the barrier capability of epoxy coating.

To further discern the mechanism of corrosion protection offered by the MAG nanofillers, the Bode data were analyzed with an electrical equivalent circuit (EEC) (Figs. S5a–c) fitting method. The EEC circuit for both epoxy-MS and MAGE-MS consisted of electrolyte resistance ($R_{\rm s}$), constant phase elements representing the coating capacitance ($Q_{\rm c}$), the coating resistance to the electrolyte ($R_{\rm c}$), the constant phase element (CPE) double layer between the steel/electrolyte ($Q_{\rm dl}$) and the Faradaic charge transfer resistance ($R_{\rm ct}$) across the steel/electrolyte interface. The epoxy-MS included additional elements of diffusion resistance ($R_{\rm diff}$), CPE diffusion element ($Q_{\rm diff}$) and a finite Warburg resistance (W). We used CPE to account for the heterogeneities offered by the biofilm

and corrosion products on the coated steel surface [42]. The capacitance (C_c) was determined based on the value of Q_c using equation (4) based on the parallel resistance method [6,45]. Similar equation was used to calculate the double layer capacitance (C_{dl}) using values of Q_{dl} .

$$C_c = R_c^{(1-n)/n} Q_c^{1/n} \tag{4}$$

where n represents the exponent in the constant phase element.

A qualitative analysis of EEC gave information on different electrochemical processes occurring at the steel/coating/electrolyte interface. The behavior of MAGE-MS adhered to a two-time constant resistance (R)-capacitance (C) circuit (as shown in Fig. S5a) throughout the exposure time. However, the circuit elements for epoxy-MS varied for different exposure times (Figs. S5b and c) indicating gradual deterioration of the coating. The EEC for epoxy-MS evolved from the two-time circuit on day 1 (Fig. S5a) to three-time constant circuit on day 10 and 20 (Fig. S5b). For day 30 and 40, the EEC included a Warburg diffusion element (Fig. S5c) account for the diffusion of corrosive ion (HS⁻ and H⁺) through pores of the epoxy coating.

Next, we compared the total corrosion resistance $(R_{corr} = R_c + R_{ct})$ of MAGE-MS and epoxy-MS obtained from the EEC fitting analysis (Fig. 7d). The R_c values indicate resistance against ionically conducting pathways in the coating while the R_{ct} is the resistance against charge transfer occurring at metal interface. Higher values of R_{corr} implies lower susceptibility to corrosion. The MAGE-MS consistently showed higher R_{corr} compared to the epoxy-MS throughout the 40 days of exposure. For example, on day

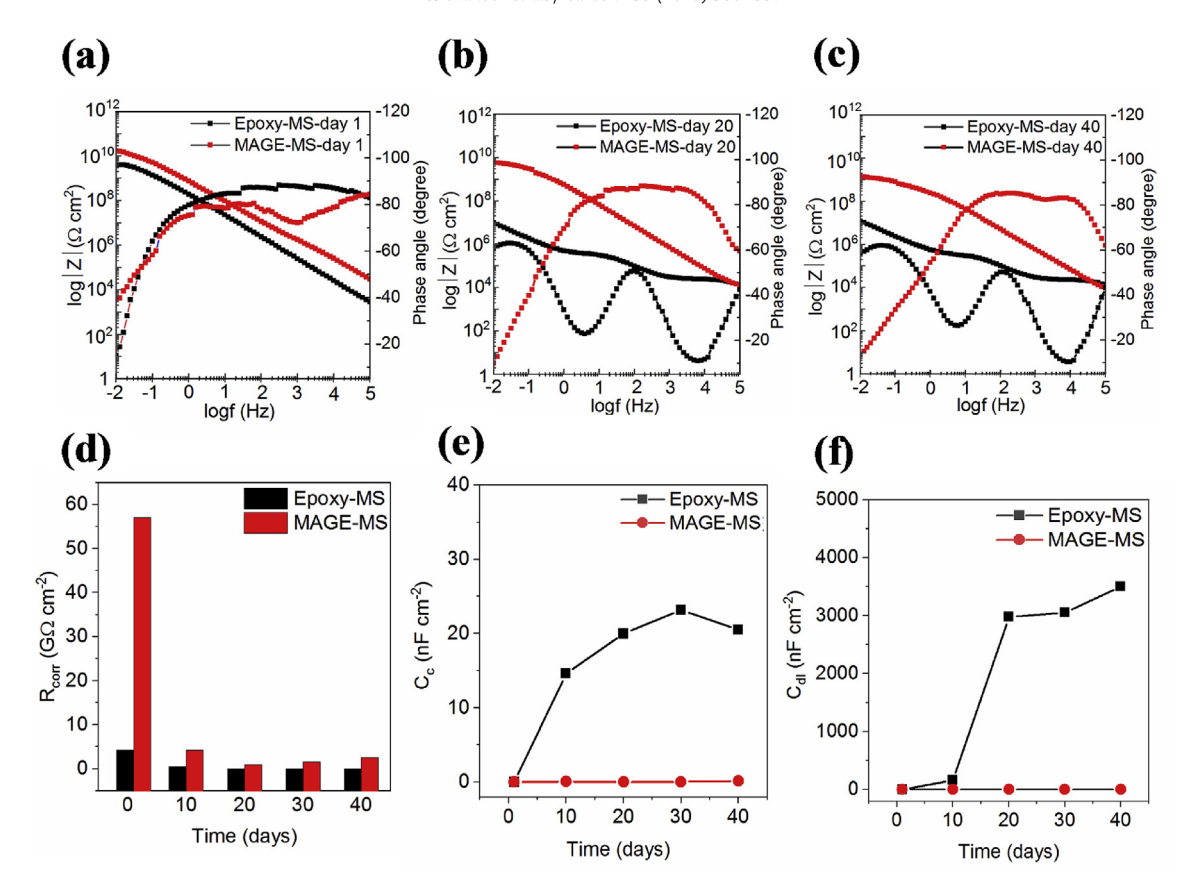


Fig. 7. Electrochemical impedance spectroscopy establishes superior microbial corrosion resistance mechanism of MAGE coatings. Bode plots for the epoxy and MAGE coated carbon steel coupons on (a) day 1 (b) day 20 and (c) day 40 using an applied sinusoidal AC potential of 10 mV and in the scanning frequency of $0.01-10^5$ Hz. The Bode phase angle plot for epoxy-MS showed significant variation in time constants after 10 days of exposure to SRB-G20. However, MAGE-MS showed two-time constants throughout the exposure period. Temporal data shows lower capacitance and higher corrosion resistance values for MAGE-MS compared to epoxy-MS indicating lower water diffusion through the coating and higher faradaic resistance at metal-coating interface. (d) Corrosion resistance (R_{corr}). (e) Coating capacitance and (f) Double layer capacitance (C_{d1}). Proposed corrosion protection mechanism for MAG nanofillers in epoxy coating. (g) Epoxy-MS and (h) MAGE-MS. Epoxy coating develop porosity during curing. The MAG nanofiller disperses uniformly in the epoxy matrix filling the defects such as voids and cracks which occurs during the curing process. Additionally, the high aspect ratio of MAG nanofillers reduces the use of filler to a low loading of <1 wt%. (A colour version of this figure can be viewed online.)

1, the R_{corr} for MAGE-MS was 410% higher compared to epoxy-MS; on day 10, 20 and 30, the R_{corr} values for MAGE-MS maintained at least two orders of magnitude higher corrosion resistance; and finally on day 40, the R_{corr} for MAGE-MS was four orders of magnitude higher (Fig. 7d). The goodness of fit for the values obtained from EEC fit shows Chi-square ($\rm X^2$) in the range of 1.25×10^{-2} to 8.8×10^{-4} . The R_{corr} values were further utilized to calculate the coating protection efficiency (using equation (5)) of MAGE-MS and epoxy-MS. The coating protection efficiency of MAGE-MS was 99.9% while the epoxy-MS registered only 91.1%.

Coating protetoion efficiency =
$$\frac{(R_{corr,coated} - R_{corr,bare})}{R_{corr,coated}} X 100$$
(5)

Next, we compared the temporal values of C_c and C_{dl} for the MAGE and epoxy coatings (Fig. 7e and f). These parameters represent the water uptake and thus their ability to allow permeate electrolytes onto the underlying steel surface [6,42]. A higher coating capacitance is typically characterized by higher volume fraction of water and higher diffusion kinetics [43,44]. Equation (6) allows the visualization of coating capacitance (C_c) as a function of the exposed coating area (A), coating thickness (d), dielectric constant of the medium (ϵ) the and free space permittivity (ϵ_0).

$$C_c = \frac{\varepsilon \varepsilon_0 A}{d} \tag{6}$$

The C_c offered by epoxy-MS was an order of magnitude higher compared to MAGE-MS (Fig. 7e and f). Further, the temporal profile of C_c for epoxy-MS exhibited significant variations (e.g., 0.9 nF/cm^2 on day $1-15 \text{ nF/cm}^2$ on day 10) (Fig. 7e). In contrast, MAGE-MS displayed a consistent C_c profile (0.01 nF/cm^2 on day 1 to 0.15 nF/cm^2 on day 40) (Fig. 7e). At end of the experiment on day 40, the C_c of MAGE-MS was 98% lower compared to epoxy-MS, implying that MAGE constitutes a barrier against potential corrosive metabolites (HS $^-$ and H $^+$). The C_{dl} of MAGE-MS was also two orders of magnitude lower throughout the experiment. Unlike epoxy-MS, the MAGE-MS displayed a consistent temporal profile for C_{dl} (Fig. 7f). These results confirm that the interconnected network of MAG fillers remained in the exposed epoxy matrix remained in tact [8,9].

Fig. 8b depicts an overview of the protection mechanisms offered by MAGE. Briefly, SRB adheres to the epoxy on steel and forms a biofilm (Fig. 8a). The microenvironment in the biofilm allows SRB to thrive and produce biogenic metabolites (HS⁻ and H⁺) that attack the underlying steel substrates. These metabolites typically diffuse through the micropores and defects such as cracks of the epoxy and reaches the steel surface. In case of MAGE, the

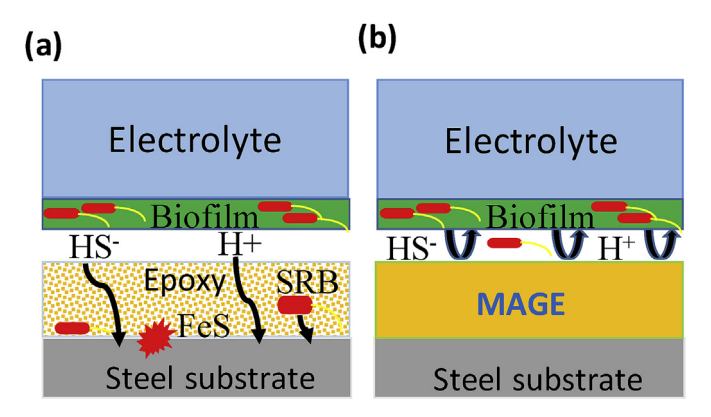


Fig. 8. Proposed corrosion protection mechanism for MAG nanofillers in epoxy coating. (a) Epoxy-MS and (b) MAGE-MS. Epoxy coating develop porosity during curing. The MAG nanofiller disperses uniformly in the epoxy matrix filling the defects such as voids and cracks which occurs during the curing process. Additionally, the high aspect ratio of MAG nanofillers reduces the use of filler to a low loading of <1 wt%. (A colour version of this figure can be viewed online.)

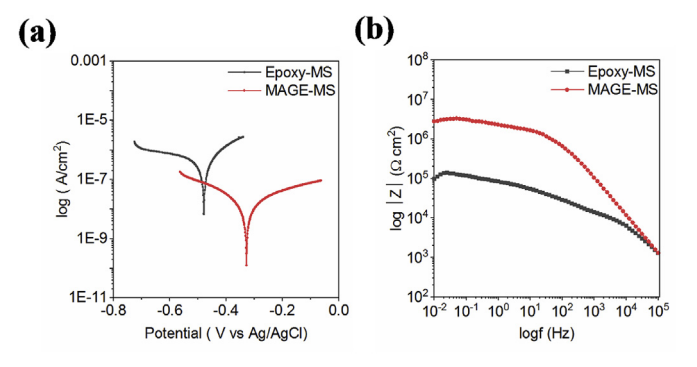
MAG molecules interconnect within the epoxy and form a barrier against corrosive metabolites. The high aspect ratio of MAG fillers yielded a higher epoxy-MAG interfacial area to create a tortuous pathway to retard diffusion of corrosive ions and prevent them from reaching the steel surface.

3.6.1. Barrier properties of MAGE in aggressive abiotic conditions (3.5% NaCl)

To further corroborate the barrier properties of MAG nanofillers, we assessed corrosion resistance of MAGE on mild steel in 3.5% NaCl compared to epoxy coating. The thickness of both the coatings was limited to 30 μm . These tests established that MAGE outperforms epoxy coating under abiotic conditions, as shown below: (i) the OCP for MAGE-MS (-327 mV vs. Ag/AgCl) was nobler compared to epoxy-MS (-479 mV vs. Ag/AgCl) (Fig. 9a); (ii) the corrosion rates of MAGE-MS (0.01 mpy) was 28- fold lower compared to epoxy-MS (0.28 mpy) (Table 1); (iii) the charge transfer resistance of MAGE-MS was two orders of magnitude higher compared to epoxy MS (obtained by fitting an EEC to the Bode plot; Fig. 9b and c, Table 2). The overall corrosion resistance of MAGE-MS was 10-fold higher compared to epoxy-MS.; and finally (iv) the coating capacitance (C_c) of the MAGE, which represents ionic pathways in coatings, was two-orders of magnitude lower compared to epoxy-MS (Table 2). These results confirm that MAGE coatings offer excellent corrosion resistance to mild steel in abiotic conditions as well as in aggressive microbial environments.

3.6.2. Outstanding performance of MAG nanofillers vs. unfunctionalized graphene fillers

We carried out additional PDP and EIS tests to assess corrosion resistance offered by maleic-anhydride-graphene adducts (vs unfunctionalized graphene nanoplatelets) to epoxy coatings on mild steel. We assessed and compared corrosion resistance of the MAGE-MS with graphene-epoxy (GE)-MS in three diverse environments, including planktonic form of SRB-G20, sessile form of SRB-G20 (Fig. S6; Table S2-S5) and 3.5% NaCl (Fig. S7; Tables S6–S7). The maleic-anhydride-graphene nanofillers outperformed unfunctionalized graphene nanoplatelets in the following manner: (i) in planktonic SRB-G20 cells, the corrosion rates of MAGE-MS (37 \times 10⁻⁶ mpy) were four orders of magnitude lower compared to GE-MS (119 \times 10⁻³ mpy); (ii) in the sessile SRB-G20 cells, the corrosion rates for MAGE-MS (4.8 \times 10⁻⁵ mpy) were



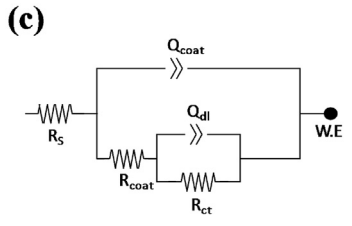


Fig. 9. Superior performance of MAGE coatings compared to epoxy coatings exposed to 3.5% NaCl. The thickness of epoxy and MAGE coatings was ~30 μm. (a) Potentio-dynamic polarization plots for epoxy-MS and MAGE-MS in a potential range of ± 250 mV from open-circuit voltage; and (b) Bode magnitude plots for epoxy-MS and MAGE-MS. Electrochemical impedance spectroscopy was carried out using a sinusoidal AC potential of 10 mV and in the frequency range of $0.01-10^5$ Hz. (c) Electrical equivalent circuit used to fit the Bode plot consisted of two pairs of resistance (R) and capacitance (C) elements connected in parallel. The first RC circuit consists of coating resistance (R_{coat}) and a constant phase element to model coating capacitance (Q_{coat}). The second RC circuit consists of charge transfer resistance (R_{coat}) and constant phase element to model double layer capacitance (Q_{cl}).

Table 1 PDP parameters for epoxy-MS and MAGE-MS in 3.5% NaCl in 3.5% NaCl after achieving steady-state OCP conditions (t = 50 min).

Sample	E_{corr} (mV)	$i_{corr}(nA\text{-}cm^{-2})$	Corrosion rate (mpy)
Epoxy-MS	-479	693	0.28
MAGE-MS	-327	32	0.01

80% lower compared to GE-MS (2.5×10^{-4} mpy) and (iii) in abiotic 3.5% NaCl, the corrosion rates of MAGE-MS (0.01 mpy) was 19-fold lower compared to GE-MS (0.19 mpy).

4. Conclusions

work demonstrates use of maleic-anhydridefunctionalized-graphene nanofillers for enhancing corrosion resistance of polymer coatings under abiotic conditions as well as in aggressive microbial conditions. We demonstrate a viable route to mechanochemically exfoliate graphite into graphene particles and functionalize their edges with maleic anhydride. Based on TEM, nanoindentation and electrochemical tests, the current study establishes following benefits of the MAGE coatings: the carbonyl and hydroxyl groups in the MAG adducts enable their dispersion in epoxy matrix, addressing typical dispersion challenges with unfunctionalized graphene platelets; the MAG nanofillers enhance the tensile and hardness property of epoxy coatings; and importantly, the imide groups in MAGE offers superb barrier properties against intercalating corrosive species into epoxy coating. All of these benefits clearly evident from the outstanding ability of MAG nanofillers in epoxy coating to effectively resist corrosion of mild steel under both abiotic and biotic conditions. The proposed

Table 2EIS parameters for epoxy-MS and MAGE-MS in 3.5% NaCl obtained after achieving steady-state OCP conditions (t = 50 min).

Sample	R _{coat} (Ω cm ²)	C _C (F cm ⁻²)	$R_{ct} (\Omega \text{ cm}^2)$	C _{dl} (F cm ⁻²)	$R_{corr} = R_c + R_{ct} (\Omega \text{ cm}^2)$
Epoxy-MS MAGE-MS	$\begin{array}{c} 1.38 \times 10^5 \\ 6.63 \times 10^5 \end{array}$	$\begin{array}{c} 1.27 \times 10^{-07} \\ 2.56 \times 10^{-09} \end{array}$	$\begin{array}{c} 1.71 \times 10^{4} \\ 8.39 \times 10^{6} \end{array}$	$\begin{array}{c} 3.81 \times 10^{-06} \\ 3.72 \times 10^{-07} \end{array}$	1.55×10^5 9.05×10^6

method is beneficial as it uses inexpensive graphite materials, mild processing conditions (ball milling) and obviates the need for harsh chemicals used in the typical solution-based exfoliation methods.

Declaration of competing interest

The authors declare that they have no known competing financial interests or personal relationships that could have appeared to influence the work reported in this paper.

CRediT authorship contribution statement

Govinda Chilkoor: Conceptualization, Methodology, Investigation, Writing - original draft, Writing - review & editing. Roman Sarder: Conceptualization, Methodology. Jamil Islam: Methodology, Validation. K.E. ArunKumar: Methodology, Validation. Ishara Ratnayake: Methodology, Validation. Shane Star: Methodology, Validation. Bharat K. Jasthi: Validation, Resources. Grigoriy Sereda: Supervision, Project administration, Writing - review & editing. Nikhil Koratkar: Validation, Writing - review & editing. M. Meyyappan: Validation, Writing - review & editing. Venkataramana Gadhamshetty: Supervision, Project administration, Writing - review & editing, Funding acquisition.

Acknowledgements

We acknowledge the funding support from National Science Foundation CAREER Award (#1454102), NSF RII Track-1: Building on the 2020 Vision: Expanding Research, Education and Innovation in SD (#1849206), NASA (NNX16AQ98A, and in part by South Dakota Board of Regents under the auspices of Surface Engineering Research Center. We thank Dr. Rajesh Sani for providing SRB-G20, Sushma P. Karanam for help with film applicator, Jacob Alderman for preparing MAGE synthesis graphic, and Todd Kurtis for help with adhesion tests.

Appendix A. Supplementary data

Supplementary data to this article can be found online at https://doi.org/10.1016/j.carbon.2019.12.059.

References

- D. Duraibabu, T. Ganeshbabu, R. Manjumeena, P. Dasan, Formulation for corrosion and microbial prevention of mild steel, Prog. Org. Coat. 77 (2014) 657–664.
- [2] G. Kobrin, S. Lamb, A. Tuthill, R. Avery, K. Selby, In microbiologically influenced corrosion of stainless steels by water used for cooling and hydrostatic testing, in: Proceedings of the International Water Conference vol 58, Engineers Society of Western Pennsylvania, 1997, pp. 504–516.
- [3] T. Unsal, T.R. Jia, S. Kumseranee, S. Punpruk, T. Gu, Laboratory investigation of microbiologically influenced corrosion of carbon steel in hydrotest using enriched artificial seawater inoculated with an oilfield biofilm consortium, Eng. Fail. Anal. 100 (2019) 544—555.
- [4] G. Chilkoor, N. Shrestha, D. Soeder, V. Gadhamshetty, Corrosion and environmental impacts during the flowback water disposal associated with the bakken shale, Corros. Sci. 133 (2018) 48–60.
- [5] G.H. Koch, M.P. Brongers, N.G. Thompson, Y.P. Virmani, J.H. Payer, Corrosion Cost and Preventive Strategies in the United States, 2002.
- [6] G. Chilkoor, S.P. Karanam, S. Star, N. Shrestha, R.K. Sani, V.K. Upadhyayula, et al., Hexagonal Boron nitride: the thinnest insulating barrier to microbial corrosion, ACS nano. ACS nano 12 (2018) 2242–2252.

- [7] T. Gu, R. Jia, T. Unsal, D. Xu, Toward a better understanding of microbiologically influenced corrosion caused by sulfate reducing bacteria, J. Mater. Sci. Technol. 35 (2019) 631–636.
- [8] G. Shi, M.Q. Zhang, M.Z. Rong, B. Wetzel, K. Friedrich, Friction and wear of low NanometerISi3N4 filled epoxy composites, Wear 254 (2003) 784–796.
- [9] T. Ramanathan, A. Abdala, S. Stankovich, D. Dikin, M. Herrera-Alonso, R. Piner, et al., Functionalized graphene sheets for polymer nanocomposites, Nat. Nanotechnol. 3 (2008) 327.
- [10] M. Xanthos, Polymers and Polymer Composites, Funct. Fillers Plast., 2010, pp. 1–18.
- [11] Y. Hayatgheib, B. Ramezanzadeh, P. Kardar, M. Mahdavian, A comparative study on fabrication of a highly effective corrosion protective system based on graphene oxide-polyaniline nanofibers/epoxy composite, Corros. Sci. 133 (2018) 358–373.
- [12] C.M. Santos, J. Mangadlao, F. Ahmed, A. Leon, R.C. Advincula, D.F. Rodrigues, Graphene nanocomposite for biomedical applications: fabrication, antimicrobial and cytotoxic investigations, Nanotechnology 23 (2012) 395101.
- [13] Y.L. Musico, C.M. Santos, M.L.P. Dalida, D.F. Rodrigues, Surface modification of membrane filters using graphene and graphene oxide-based nanomaterials for bacterial inactivation and removal, ACS Sustain. Chem. Eng. 2 (2014) 1559–1565.
- [14] S. Bian, S.A.M. Scott, Y. Cao, Y. Liang, S. Osuna, K. Houk, et al., Covalently patterned graphene surfaces by a force-accelerated diels—alder reaction, J. Am. Chem. Soc. 135 (2013) 9240—9243.
- [15] M. Terrones, O. Martín, M. González, J. Pozuelo, B. Serrano, J.C. Cabanelas, et al., Interphases in graphene polymer-based nanocomposites: achievements and challenges, Adv. Mater. 23 (2011) 5302–5310.
- [16] Y. Cao, S. Osuna, Y. Liang, R.C. Haddon, K. Houk, Diels—alder reactions of graphene: computational predictions of products and sites of reaction, J. Am. Chem. Soc. 135 (2013) 17643—17649.
- [17] J.K. Niemeier, D.P. Kjell, Hydrazine and aqueous hydrazine solutions: evaluating safety in chemical processes, org, Process Res. Dev. 17 (2013) 1580–1590.
- [18] T.H. Fang, C.H. Lee, In anti-corrosion and mechanical property of zinc modified nanocomposites, meeting abstracts, J. Electrochem. Soc. 484 (2016) 220–228, 953-953.
- [19] K. Natarajan, Antibiofilm activity of epoxy/Ag-TiO2 polymer nanocomposite coatings against Staphylococcus aureus and Escherichia coli, Coatings 5 (2015) 95—114.
- [20] C. M Santos, M.C.R. Tria, R.A.M.V. Vergara, F. Ahmed, R.C. Advincula, D.F. Rodrigues, Antimicrobial graphene polymer (PVK-GO) nanocomposite films, Chem. Commun. 47 (2011) 8892–8894.
- [21] Y. Ahmadi, S. Ahmad, Surface-active antimicrobial and anticorrosive Oleo-Polyurethane/graphene oxide nanocomposite coatings: synergistic effects of in-situ polymerization and π - π interaction, Prog. Org. Coat. 127 (2019) 168–180
- [22] A.M. Kumar, A. Khan, R. Suleiman, M. Qamar, S. Saravanan, H. Dafalla, Bifunctional CuO/TiO2 nanocomposite as nanofiller for improved corrosion resistance and antibacterial protection, Prog. Org. Coat. 114 (2018) 9–18.
- [23] C.K. Patil, H.D. Jirimali, M.S. Mahajan, J.S. Paradeshi, B.L. Chaudhari, V.V. Gite, Functional anti-corrosive and anti-bacterial surface coatings based on mercaptosuccinic and thiodipropionic acids and algae oil as renewable feedstock, Funct. Polym. 139 (2019) 142–152.
- [24] Y. Lang, Y. Sun, M. Yu, Y. Ji, L. Wang, Z. Zhang, Differential colonization dynamics of marine biofilm-forming eukaryotic microbes on different protective coating materials, Polymja 11 (2019) 161.
- [25] G. Chilkoor, V.K. Upadhyayula, V. Gadhamshetty, N. Koratkar, M. Tysklind, Sustainability of renewable fuel infrastructure: a screening LCA case study of anticorrosive graphene oxide epoxy liners in steel tanks for the storage of biodiesel and its blends, Environ. Sci. Process Impacts. 19 (2017) 141–153.
- [26] V.K. Upadhyayula, D.E. Meyer, V. Gadhamshetty, N. Koratkar, Screening-level life cycle assessment of graphene-poly (ether imide) coatings protecting unalloyed steel from severe atmospheric corrosion, ACS Sustain. Chem. Eng. 5 (2017) 2656–2667.
- [27] J. M Seo, I.Y. Jeon, J.B. Baek, Mechanochemically driven solid-state diels—alder reaction of graphite into graphene nanoplatelets, Chem. Sci. 4 (2013) 4273–4277.
- [28] R.K. Sani, G. Geesey, B.M. Peyton, Assessment of lead toxicity to Desulfovibrio desulfuricans G20: influence of components of lactate C medium, Adv. Environ. Res. 5 (2001) 269–276.
- [29] F. T Johra, J.W. Lee, W.G. Jung, Facile and safe graphene preparation on solution based platform, J. Ind. Eng. Chem. (Amsterdam, Neth.), J. Ind. Eng. Chem. 20 (2014) 2883–2887.
- [30] J. Dubois, M. Colaço, G. Rondelet, J. Wouters, Synthesis and crystallographic characterization of a maleimide derivative of tryptamine, Crystals 6 (2016)

- 153
- [31] O. Zabihi, M. Ahmadi, T. Abdollahi, S. Nikafshar, M. Naebe, Collision-induced activation: towards industrially scalable approach to graphite nanoplatelets functionalization for superior polymer nanocomposites, Sci. Rep. 7 (2017) 3560
- [32] C. Koning, A. Ikker, R. Borggreve, L. Leemans, M. Möller, Polym. Reactive Blending of Poly (Styrene-co-maleic Anhydride) with Poly (Phenylene Oxide) by Addition of Á-Amino-Polystyrene, vol 34, 1993, pp. 4410–4416.
- [33] E. Jafari, Synthesis and evaluation of antimicrobial activity of cyclic imides derived from phthalic and succinic anhydrides, Res. Pharm. Sci. 12 (2017) 526.
- [34] M. Bhattacharya, Polymer nanocomposites—a comparison between carbon nanotubes, graphene, and clay as nanofillers, Materials 9 (2016) 262.
- [35] Y.J. Noh, H.I. Joh, J. Yu, S.H. Hwang, S. Lee, C.H. Lee, S.Y. Kim, J.R. Youn, Ultrahigh dispersion of graphene in polymer composite via solvent free fabrication and functionalization, Sci. Rep. 5 (2015) 9141.
- [36] A.V. Dudchenko, C. Chen, A. Cardenas, J. Rolf, D. Jassby, Frequency-dependent stability of CNT joule heaters in ionizable media and desalination processes, Nat. Nanotechnol. 12 (2017) 557.
- [37] S.M. Skovhus, L.T. Caffrey, Applications of Molecular Microbiological Methods, Caister Academic Press, Norfolk, UK, 2014.
- [38] G. Chilkoor, N. Shrestha, S.P. Karanam, V.K. Upadhyayula, V. Gadhamshetty,

- Graphene coatings for microbial corrosion applications, Encycl. Water: Sci. Technol. Soc. (2019), https://doi.org/10.1002/9781119300762.wsts0125.
- [39] D. Pavithra, M. Doble, Biofilm formation, bacterial adhesion and host response on polymeric implants issues and prevention, Biomed. Mater. 3 (2008), 034003.
- [40] A. Krasowska, K. Sigler, How microorganisms use hydrophobicity and what does this mean for human needs? Front, cell. infect, mi. 4 (2014) 112.
- [41] Y.H. An, R.J. Friedman (Eds.), Handbook of Bacterial Adhesion: Principles, Methods, and Applications, Humana Press, NJ, 2000.
- [42] R. Jia, J. L Tan, P. Jin, D.J. Blackwood, D. Xu, T. Gu, Effects of biogenic H2S on the microbiologically influenced corrosion of C1018 carbon steel by sulfate reducing Desulfovibrio vulgaris biofilm, Corros. Sci. 130 (2018) 1–11.
- [43] F. Deflorian, L. Fedrizzi, S. Rossi, P. Bonora, Organic coating capacitance measurement by EIS: ideal and actual trends, Acta 44 (1999) 4243–4249.
- [44] F. Deflorian, L. Fedrizzi, P. Bonora, Influence of the Photo-oxidative degradation on the water barrier and corrosion protection properties of polyester paints, Corros. Sci. 38 (1996) 1697—1708.
- [45] N. Waters, R. Connolly, D. Brown, B. Laskowski, in: Electrochemical Impedance Spectroscopy for Coating Evaluation Using a Micro Sensor, Annual Conference of the Prognostics and Health Management Society, Fort Worth, TX, Oct 2014.